

# The Next Generation of Colloidal Probes: A Universal Approach for Soft and Ultra-Small Particles

Andreas Mark, Nicolas Helfricht, Astrid Rauh, Matthias Karg, and Georg Papastavrou\*

The colloidal probe technique, which is based on the atomic force microscope, revolutionizes direct force measurements in many fields, such as interface science or biomechanics. It allows, for the first time, interaction forces on the single particle or cell level to be determined. However, for many applications, important “blind spots” remain, namely, the possibility to probe interaction potentials for nanoparticles or complex colloids with a soft outer shell. Definitely, these are colloidal systems that are currently of major industrial importance and interest from theory. The here-presented novel approach allows the aforementioned limitations to be overcome. Its applicability is demonstrated for 300 nm sized carboxylate-modified latex particles as well as sub-micron core-shell particles with a soft poly-*N*-isopropylacrylamide hydrogel shell and a rigid silica core. For the latter, which until now could not be studied by the colloidal probe technique, the temperature dependency of electrosteric and adhesion forces is determined on the single particle level.

SFA. With the advent of the colloidal probe technique also atomic force microscopy (AFM) could be adapted for the quantitative measurement of interaction forces.<sup>[7,8]</sup> The “classical” colloidal probe technique makes use of a single colloidal particle, which is permanently glued to the end of an AFM cantilever. Commonly, these particles have diameters in the range of several micrometers and are often made from silica<sup>[8,9]</sup> or poly(styrene).<sup>[10]</sup> However, also soft objects, like hydrogel beads, can be utilized as colloidal probes.<sup>[11,12]</sup> The interaction geometry in AFM experiments is not limited to the sphere versus flat surface (i.e., sphere/plane) and also direct force measurements between colloidal particles in the sphere/sphere geometry have been reported.<sup>[13–15]</sup>

## 1. Introduction

Direct force measurements became an essential analytical technique in colloid and interface science.<sup>[1–5]</sup> Initially, these measurements could only be performed with the surface force apparatus (SFA). The SFA is based on two crossed mica cylinders with centimeter dimensions and requires samples of extremely low surface roughness.<sup>[6]</sup> In consequence, only a limited number of colloidal systems are suitable to be studied by

The colloidal probe technique is utilized in many laboratories worldwide and typical applications range from determining adhesion behavior,<sup>[16,17]</sup> to mechanical properties,<sup>[18,19]</sup> or colloidal interaction forces.<sup>[5]</sup> Nevertheless, the essential preparation procedure for colloidal probes has not seen significant changes in the last 30 years:<sup>[20,21]</sup> Shortly, a colloidal particle is placed by means of a micromanipulator (or the AFM) at the end of a tipless cantilever, where it is immobilized permanently, either by glue or by a sintering procedure.<sup>[22]</sup> Hence, obtaining statistically significant datasets requires the preparation of a large number of colloidal probes. Moreover, surface modification of the probe particles after preparation is highly problematic due to the extremely small surface area involved. The latter limitation can be resolved by the multiple-colloidal probe technique,<sup>[5]</sup> which is based on the in situ immobilization of colloidal particles onto a chemically modified cantilever. Thereby, measurements can be carried out in colloidal suspensions. Hence, this technique is taking advantage of the large surface to volume ratio and provides the possibility to prepare in situ a large number of colloidal probes in order to obtain a statistically relevant number of measurements in a manageable time frame. However, particle immobilization is only possible for certain types of colloidal particles, which have a suitable surface chemistry. Moreover, the multiple-colloidal probe technique requires “hard” colloidal particles for the attachment process since the particle and cantilever are pressed onto each other in order to initiate the immobilization.<sup>[5]</sup>

Despite the large success of the colloidal probe technique, it becomes increasingly evident that the technique in its present form has currently some “blind spots”: namely, the impossibility to utilize sub- $\mu\text{m}$ -sized particles as probes or the missing option to attach particles with a soft outer shell to the surface of a cantilever. Unfortunately, nanometer-sized colloids

A. Mark, Dr. N. Helfricht, Prof. G. Papastavrou  
Physical Chemistry II  
University of Bayreuth  
Universitätsstr. 30, 95440 Bayreuth, Germany  
E-mail: Georg.Papastavrou@uni-bayreuth.de

Dr. N. Helfricht, Prof. G. Papastavrou  
Bavarian Polymer Institute  
University of Bayreuth  
Universitätsstr. 30, 95440 Bayreuth, Germany

Dr. A. Rauh, Prof. M. Karg  
Department of Physical Chemistry I  
Heinrich-Heine-University  
Universitätsstr. 1, 40204 Düsseldorf, Germany

 The ORCID identification number(s) for the author(s) of this article can be found under <https://doi.org/10.1002/sml.201902976>.

© 2019 The Authors. Published by WILEY-VCH Verlag GmbH & Co. KGaA, Weinheim. This is an open access article under the terms of the Creative Commons Attribution-NonCommercial-NoDerivs License, which permits use and distribution in any medium, provided the original work is properly cited, the use is non-commercial and no modifications or adaptations are made.

The copyright line for this article was changed on 28 September 2019 after original online publication.

DOI: 10.1002/sml.201902976

as well as those with soft shells represent currently the most relevant colloidal systems for industrial applications. The combination of nanofluidics with AFM, in the following referred to as FluidFM-technology,<sup>[23]</sup> allows for a revolutionary new approach toward the preparation of colloidal probes.<sup>[15,24,25]</sup> Instead of gluing or sintering particles permanently onto the cantilever, the particles can be aspirated in situ and in a temporary manner to the aperture of a hollow, micro-channeled AFM cantilever.<sup>[15,24,25]</sup> Hence, FluidFM-technology provides the same advantages as the multiple-colloidal probe technique in terms of direct force measurements, but it imposes much less limitations in terms of particle size and surface chemistry as neither optical manipulation nor chemical modification of the cantilever are required. Very recently, we showed that the FluidFM-technique can be extended to particles with a diameter in the order of 500 nm.<sup>[15]</sup> However, our previous experiments have been carried out only with silica particles. These provided a number of advantages for the initial experiments: they are representing the most commonly used colloidal probes,<sup>[20,21]</sup> they have a well-known surface chemistry,<sup>[26]</sup> and do not deform under external forces in the nN-regime.

Here, we demonstrate that the FluidFM-technology can provide a more general approach to the colloidal probe technique. For the first time, we prepare colloidal probes from latex particles with a diameter in the order of 300 nm. Such particles represent a model system for the wide class of small colloidal particles prepared by emulsion polymerization, which are extensively used in industrial formulations, in particular after surface modification.<sup>[27–29]</sup> Moreover, we demonstrate that also core-shell particles with rigid cores and soft, deformable hydrogel shells are accessible as colloidal probes by means of the FluidFM-technology. Such core-shell particles received currently much attention due to their unique behavior at interfaces

and the possibility to tune the interaction by means of external stimuli.<sup>[30–34]</sup> To the best of our knowledge, comparable core-shell particles have never been utilized as colloidal probes before.

## 2. Results and Discussion

Figure 1a shows a schematic representation of the experimental setup, which allows to perform direct force measurements with colloidal particles that are immobilized in a temporary manner to the cantilever by aspiration.<sup>[15,24,25]</sup> The essential components comprise an AFM cantilever with an internal micro-channel and a pressure controller with a pressure range of  $-800$  to  $+1000$  mbar. The free end of the micro-channeled cantilever bears an opening, in the following referred to as aperture. This aperture is pivotal in order to immobilize colloidal particles to the cantilever. Otherwise, the instrument is based on exactly the same principles as a “conventional” AFM. A scanning electron microscopy (SEM) image of a representative micro-channeled cantilever, which has been used in our experiments is shown as inset in Figure 1a. In order to visualize the internal structure of the micro-channel, a part of the cantilever has been selectively removed by focused ion beam milling (FIB). All cantilevers used had a pyramidal tip bearing an aperture with a nominal diameter of  $\approx 300$  nm, which is shown in Figure 1b.

### 2.1. Aspiration of Colloidal Particles

The complete process of aspirating and releasing particles by the FluidFM-technique is schematically depicted in Figure 1c. First, the channel of the FluidFM-cantilever has been completely

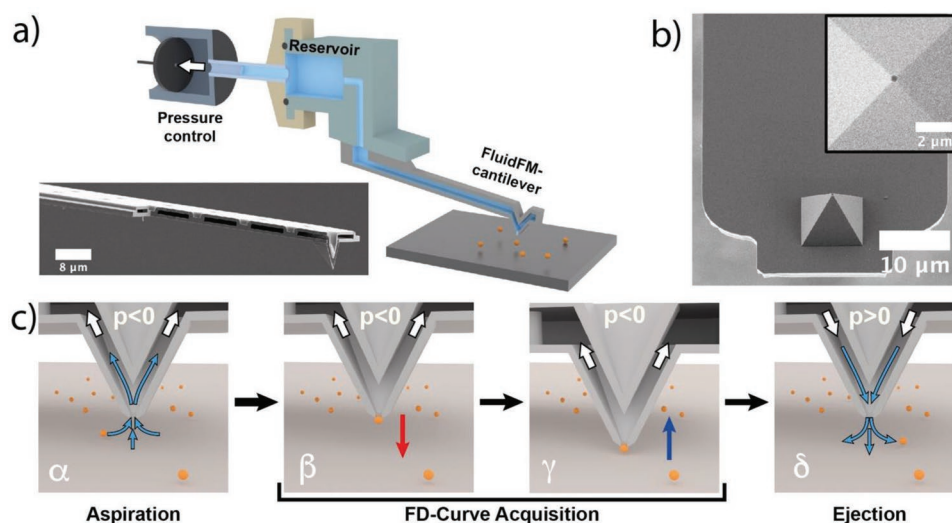


**Figure 1.** Aspiration of nanoparticles at the aperture of a cantilever with an internal micro-channel. a) Schematic representation of the experimental setup. The inset shows an SEM image of a cantilever with a micro-channel. In order to visualize the internal channel, material has been removed by FIB. b) SEM image of the pyramidal tip at the end of the cantilever. The aperture has a diameter of approximately 300 nm. c) Schematic illustration of particle aspiration and immobilization process. White arrows indicate the externally applied pressure and light blue arrows the resulting liquid flow. α) Aspiration of a particle is performed by applying a pressure  $p_{asp}$ . After a particle is immobilized at the aperture, a hold pressure of  $p_{hold}$  is applied and force versus distance curves are acquired, where β, γ) red and blue arrows indicate the approach and withdraw part of force versus distance curves, respectively. Finally, δ) the particle is ejected from the aperture by applying an over-pressure pulse.

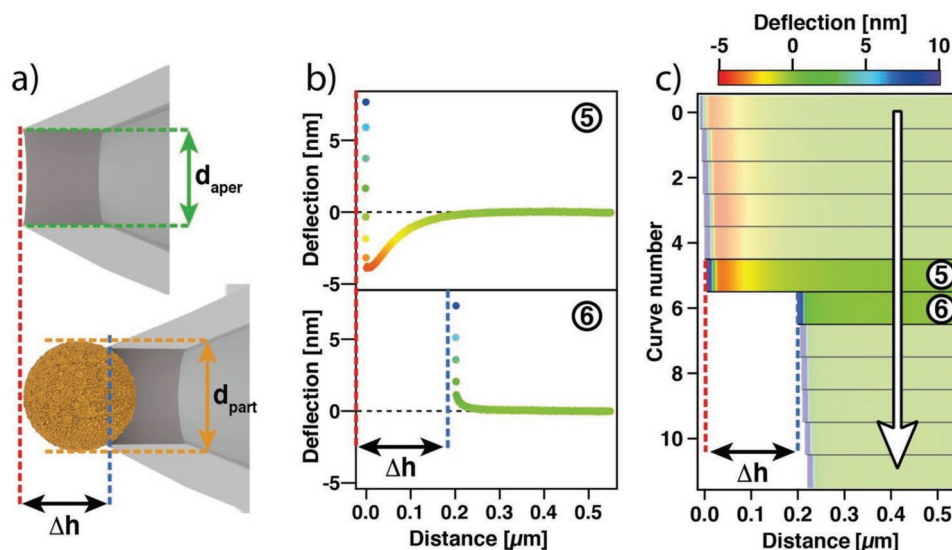


**Figure 2.** Detection of particle aspiration. a) Schematic representation of the aperture *before* and *after* aspirating a colloidal particle, respectively. b) Deflection versus distance curves *before* and *after* a particle has been immobilized at the aperture. c) False color representation of consecutively acquired deflection versus distance curves. Particle aspiration can be detected by a characteristic shift in separation  $\Delta h$ .

filled with the same electrolyte solution as present in the liquid cell. Then, the micro-channelled cantilever has been immersed in a highly diluted suspension of colloidal particles, while being placed several hundreds of nanometers above the sample surface. By applying a sufficiently high under-pressure (see white arrows), a liquid stream toward the aperture of the cantilever has been induced (see light blue arrows in Figure 1c- $\alpha$ ). Due to the applied under-pressure, also particles present in the electrolyte solution have been pulled with the liquid toward the aperture. Hence, a single particle has been immobilized in the aperture at a certain moment ( $\beta$ ). By applying a holding pressure, a series of force versus distance curves could be measured ( $\beta, \gamma$ ). This holding pressure prevented movement or loss of the particle upon contact with the sample surface during direct force measurements. Finally, the particle could be removed by application of an over-pressure pulse (e.g., +1000 mbar) to retain an open aperture ( $\delta$ ). The complete procedure with the steps  $\alpha$ – $\delta$  can be repeated several times for different colloidal particles. Thus, it provides the possibility to obtain a statistically relevant number of measurements with different colloidal probes using the same cantilever, analogous to the multiple-colloidal probe technique.<sup>[5]</sup>

## 2.2. Detection of Particle Aspiration

The successful aspiration of particles can be verified by optical microscopy only for sufficiently large particles, typically with diameters larger than 2  $\mu\text{m}$ . Hence, indirect methods have to be applied for smaller particles. Recently, Helfricht et al. presented a method based on continuously acquiring deflection versus distance curves (see Figure 2).<sup>[15]</sup> Upon particle aspiration, the aperture is “blocked” and the tip-sample separation is increased by  $\Delta h$  due to the immobilized particle, which has the diameter  $d_{\text{part}}$ . As the particle is partially sitting inside the

aperture with  $d_{\text{aper}} < d_{\text{part}}$ , one finds  $\Delta h < d_{\text{part}}$  (see Figure 2a). Figure 2b,c illustrate how the characteristic shift  $\Delta h$  can be directly detected from consecutively acquired deflection versus distance curves. In Figure 2b, exemplary deflection versus distance curves upon approach are shown for an open and blocked aperture, respectively. The interaction profiles changed significantly when a particle gets aspirated and thus blocks the aperture. For an open aperture (see curve 5, Figure 2b), tip-sample interactions are mainly governed by long-ranged attractive forces of hydrodynamic origin, caused by the liquid stream toward the aperture.<sup>[15]</sup> By contrast, if the aperture is blocked by an aspirated particle (see curve 6, Figure 2b), the interaction force profile is dominated by repulsive forces due to the overlap of diffuse layers originating from both negatively charged surfaces, namely, the carboxylate-modified latex (CML) bead and the glass substrate.<sup>[10]</sup> These forces are of electrostatic origin and much shorter ranged than the hydrodynamic forces during aspiration with an unblocked aperture. The forces for a blocked aperture are compatible with DLVO-theory by Derjaguin, Landau, Verwey, and Overbeek.<sup>[11]</sup> The consecutively acquired raw data, i.e., cantilever deflection versus distance, can be visualized directly in a false color representation (see Figure 2c). In the example shown, the first six curves (top to bottom) were acquired with an open aperture. Between force curve numbers 5 and 6, a particle has been aspirated, leading to the characteristic shift  $\Delta h$  of the contact point, which is directly visible in the distance covered by the piezo actuator. The subsequent curves show a shift by  $\Delta h$  for the onset of the contact region. Hence, indicating that the particle is retained in the aperture by the applied under-pressure (here:  $p_{\text{asp}} = -600$  mbar). The slight shift between consecutive curves in the false-color representation can be attributed to thermally induced drift of the cantilever. The drift seems to be especially pronounced for the sandwich structure of the cantilevers with an internal micro-channel. These variations are only visible for the

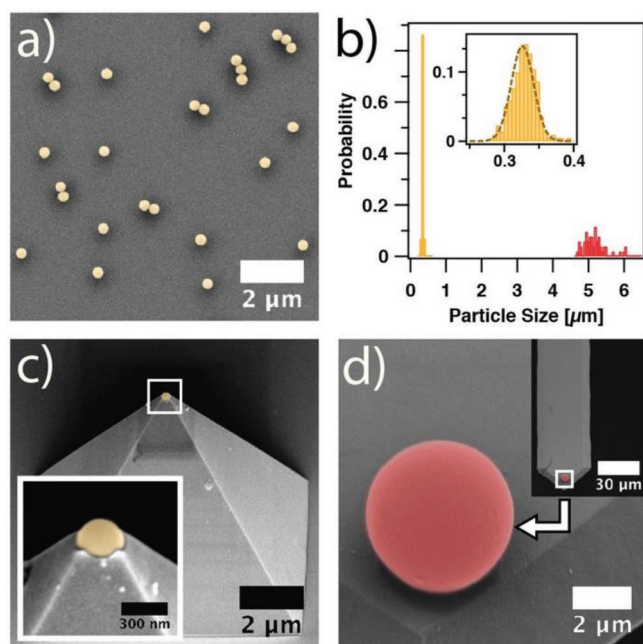


**Figure 3.** Comparison of macroscopic and nanoscopic colloidal probes. a) SEM image of CML particles. b) Size distribution of “small” (330 nm) and “large” (5.06  $\mu\text{m}$ ) CML particles as obtained by SEM. c) SEM image of a single “small” CML particle aspirated at the 300 nm aperture of a micro-channelled AFM cantilever. The inset shows a magnification of the particle partially hidden in the aperture. d) A “classical” colloidal probe from a “large” CML particle, which has been glued to a “standard” tipless AFM cantilever without internal channel.

raw data and are not significant for the resulting interaction force profile.

### 2.3. Direct Force Measurements with 330 nm Sized Particles

CML particles represent a model system for colloids synthesized by emulsion polymerization.<sup>[35,36]</sup> Such particles are an essential part of many industrial formulations as their surface chemistry can be easily modified for specific applications.<sup>[27,28]</sup> The SEM image in **Figure 3a** shows several CML particles, which have been deposited onto a silicon wafer. The corresponding size distribution for these particles, as obtained from SEM images, is shown in **Figure 3b** and the corresponding inset (yellow histograms). We found an average diameter of  $326 \pm 16$  nm, which is in good agreement with the value provided by the manufacturer ( $330 \pm 13$  nm).

**Figure 3c** gives an impression of how a colloidal probe with an aspirated CML particle looks in situ. In order to obtain this SEM image, we removed the FluidFM-cantilever from solution, while a particle has been aspirated and hold in place by a constant under-pressure  $p_{\text{asp}}$ . After drying, the cantilever has been imaged by SEM. The debris visible in **Figure 3c** results most likely from the transfer of the probe through the liquid/air interface. In order to illustrate the dimensions of nm-sized colloidal probes prepared here, we show in **Figure 3d** for direct comparison an SEM image of a “classical” colloidal probe that has been prepared by gluing a “large” CML particle to a

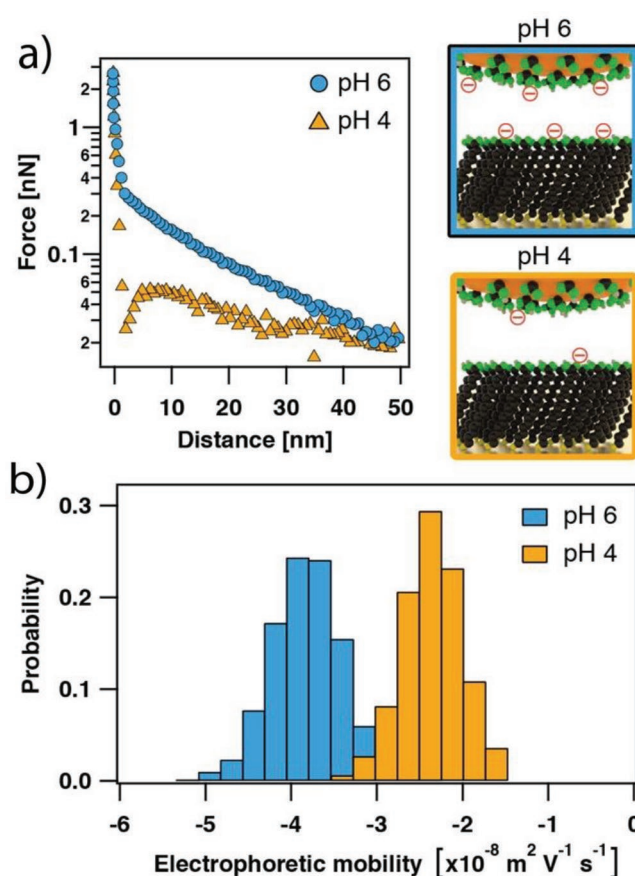


**Figure 4.** Surface charge of CML nanoparticles. a) Force profiles upon approach showing long-range electrostatic interactions of a 330 nm sized CML particle versus a surface bearing a COOH-terminated SAM. The force profiles have been acquired at pH 4 (orange) and pH 6 (blue), respectively, with a total ionic strength of  $I = 0.1 \times 10^{-3}$  M. The small images illustrate the surface charges at the different pH-values in a schematic manner. b) Distribution of the electrophoretic mobilities of the 330 nm sized CML particles at pH 6 and pH 4, respectively ( $I = 0.1 \times 10^{-3}$  M).

standard tipless AFM cantilever. These “large” CML particles have an average diameter of  $5.06 \pm 0.22$   $\mu\text{m}$  as shown in the corresponding size distribution (red histogram) in **Figure 3b**.

**Figure 4a** shows some exemplary force versus distance curves, which have been acquired with the small 330 nm sized CML particles as colloidal probe. Long-range interaction forces have been determined versus a flat gold substrate, which has been modified by a self-assembled monolayer (SAM) of thiols, terminating in carboxyl groups. Likewise, the CML particles bear a high density of carboxyl groups at their surface. Hence, the interaction forces between the surfaces should strongly depend on the pH of the electrolyte solution: with increasing pH, the ionization state of the COOH-groups is increasing and thus the repulsive force of electrostatic origin should increase.<sup>[37,38]</sup> The expected charging states of both surfaces are shown schematically as insets. In **Figure 4a**, the corresponding approach parts of the force versus distance curves are shown for pH 4 and pH 6, respectively. The total ionic strength has been adjusted to  $0.1 \times 10^{-3}$  M for all pH values. The force profiles are shown in a semi-logarithmic representation and are

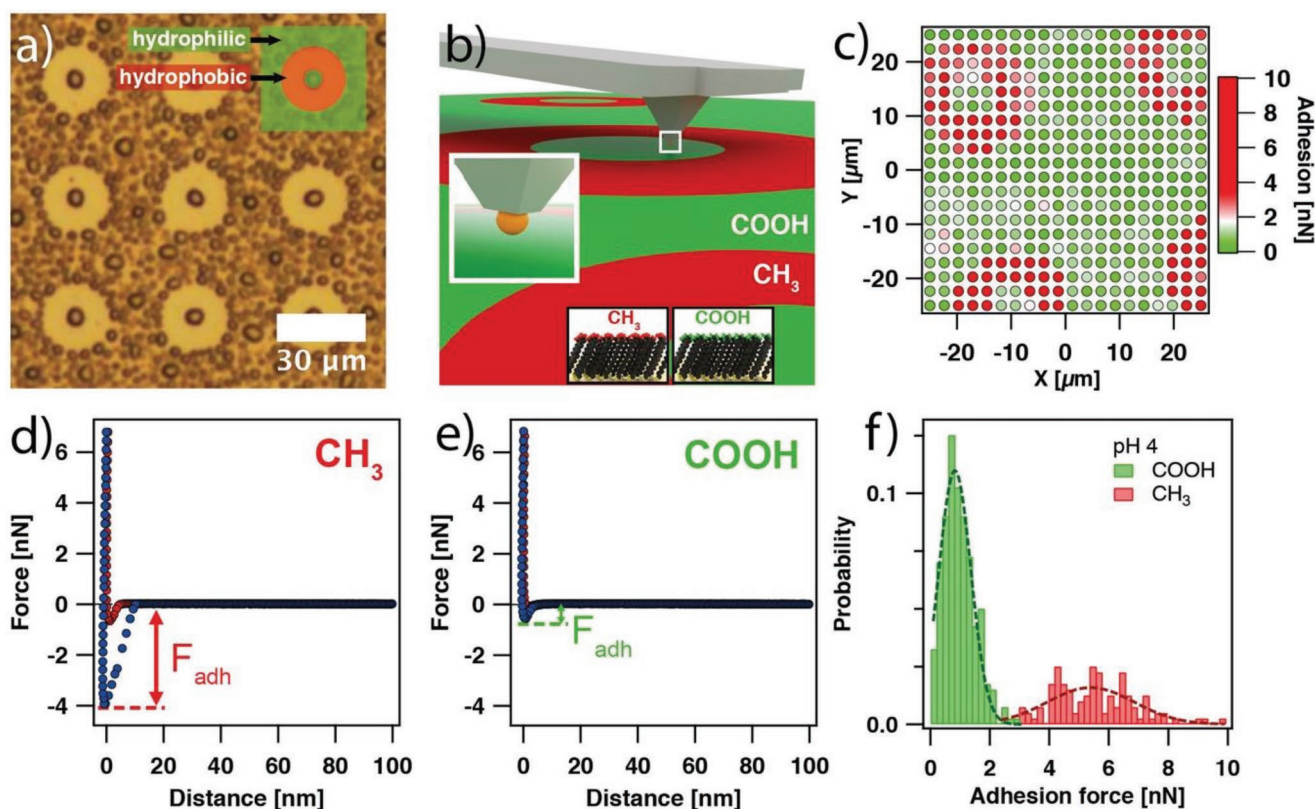


**Figure 5.** Adhesion properties of CML nanoparticles. a) Condensation microscopy image (“breathing figure”) of the chemically structured sample. The inset depicts the distribution of hydrophilic (green) and hydrophobic (red) regions on the sample. b) Schematic illustration of the experimental setup for the lateral mapping of adhesion forces between an aspirated nanoparticle and chemically structured samples. c) Representation of the lateral distribution of adhesion forces on the structured samples. Red corresponds to high adhesion forces. d,e) Exemplary force versus distance curves for a CML particle as determined at pH 4 on a CH<sub>3</sub>- and a COOH-modified surface, respectively. The red and blue data points correspond to the approach and withdraw part of the force curve, respectively. f) Histogram of the adhesion forces acquired on a structured sample. The dashed lines are a guide to the eye illustrating the fit to a Gaussian distribution.

based on data averaged from more than 50 individual force curves. For both pH values, the interaction force profiles are repulsive at large separation distances. The linear slope in the semi-logarithmic representation indicates a decay with the Debye-length for both pH values and is expected for electrostatic repulsion due to diffuse layer overlap of the negatively charged carboxylate-terminated surfaces.<sup>[3,13]</sup> However, the interaction is significantly more repulsive for the force profiles acquired at pH 6 due to the higher diffuse layer potentials originating from the larger degree of ionization for the COOH-groups at pH 6. By contrast, carboxyl groups are almost fully protonated at pH 4, thus resulting only in slightly negatively charged surfaces. The charging state of COOH-terminated SAMs has been extensively studied by means of contact angle titrations,<sup>[37]</sup> streaming potential,<sup>[39]</sup> and direct force measurements, respectively.<sup>[38]</sup> In comparison to a single isolated carboxyl group with  $pK_a = 4.8$  (see, e.g., ref. [40]), the  $pK_a$  for a COOH-terminated SAM is approximately  $pK_a = 6.3$ .<sup>[41]</sup> The latter  $pK_a$  is also valid for the carboxyl groups on the CML particles used as colloidal probes. The data from direct force measurements have been corroborated by electrophoretic mobility measurements of the CML particles at identical pH and ionic strength (see Figure 4b). The electrophoretic mobility data are in line with other studies for COOH-modified latex particles.<sup>[42]</sup>

#### 2.4. Adhesion Behavior of nm-Sized Particles

As small colloidal particles are increasingly used in paints or adhesion promoters,<sup>[27]</sup> their interfacial behavior represents an essential parameter for optimizing the formulations. Thus, the ability to determine adhesion forces on the level of single nanoparticles becomes increasingly important. Here, we demonstrate a proof of concept for chemically heterogeneous surfaces. Such surfaces with highly defined chemical functionalities have been prepared by micro-contact printing ( $\mu$ CP).<sup>[43,44]</sup> Well-defined patterns of hydrophobic and hydrophilic regions have been obtained by  $\mu$ CP with CH<sub>3</sub>- and COOH-terminated thiols. In order to verify the chemical structure of the surfaces after  $\mu$ CP, various analytical techniques have been utilized: a breathing figure based on different water condensation behavior on hydrophobic and hydrophilic areas, respectively, is presented in Figure 5a. The darker spots in the optical microscopy image correspond to hydrophilic regions with increased water condensation, while the brighter ring-like structures are hydrophobic and thus prevent condensation of water. The data obtained by further techniques, such as mapping of adhesion forces by AFM PeakForce mode in liquid and SEM imaging are given in the Supporting Information.

The experimental approach that has been used here for mapping adhesion forces of nanoparticles on  $\mu$ CP-structured

substrates is schematically shown in Figure 5b. Force versus distance curves have been acquired in a grid of lateral positions, so-called force volume plots.<sup>[3,45]</sup> Here, we concentrate on the adhesion force, i.e., the force required to remove the aspirated particle from the substrate. Figure 5c summarizes the adhesion forces for a 330 nm sized CML particle measured on an area of 50 μm × 50 μm. Red spots indicate areas with high adhesion forces, while green spots indicate weak adhesion, respectively. The resulting pattern of adhesion forces reflects exactly the distribution of the CH<sub>3</sub>- and COOH-terminated areas as prepared by μCP and verified independently by other techniques (see Figure 5b and the Supporting Information): the round doughnut-shaped regions (i.e., the red regions in Figure 5c) terminate in the hydrophobic CH<sub>3</sub>-groups, while the rest of the gold substrate is terminating in hydrophilic COOH-groups.

Figure 5d,e shows representative force versus distance curves for the two different chemical terminations on the μCP-structured substrates. Each force profile shows the approach part (red) as well as the retraction part (blue) and represents an average from at least 50 individual force profiles. Figure 5f shows the distribution of the adhesion forces, as indicated by arrows in Figure 5d,e. The histogram in Figure 5f represents all adhesion forces determined during one force volume measurement acquired on the structured substrate (see Figure 5c). The presence of two distinctly different chemical functionalities terminating these regions is reflected by the bi-modal distribution of the adhesion forces; similar results have been obtained by chemical force microscopy where the tip of the cantilever is modified by SAMs.<sup>[44,46–48]</sup>

In the adhesion distribution shown in Figure 5f, the first maximum ( $F_{\text{exp}} = 0.92 \pm 0.54$  nN) corresponds to the hydrophilic COOH-terminated regions and the second maximum ( $F_{\text{exp}} = 5.39 \pm 1.46$  nN) to the hydrophobic CH<sub>3</sub>-terminated regions. According to Johnson, Kendall, and Roberts (JKR)-theory, the adhesion force  $F_{\text{JKR}}$  is given by  $F_{\text{JKR}} = \frac{3}{2}\pi W_{\text{adh}}R$ . Here,  $R$  is the radius of the probe particle and  $W_{\text{adh}}$  is the work of adhesion, which is given by  $W_{\text{adh}} = \gamma_{\text{CML}/\text{H}_2\text{O}} + \gamma_{\text{SAM}/\text{H}_2\text{O}} - \gamma_{\text{CML}/\text{SAM}}$ .<sup>[3,46]</sup> The resulting normalization of the experimental adhesion forces  $F_{\text{exp}}$  by the average radius of the colloidal particles  $R$  (see inset in Figure 3b) is shown in the first column of Table 1. These values are in good quantitative agreement with estimations based on literature values for the interfacial energies  $\gamma$  within the framework of the JKR-theory.<sup>[17,46,47,49]</sup> With the values for the interfacial energies reported by Sinniah et al. and Warszyński et al. (see compilation in the Supporting Information),<sup>[46,47]</sup> one obtains  $F_{\text{JKR}}/R$ . At pH 4, the electrostatic interactions are largely suppressed and adhesion is dominated by solvent exclusion.<sup>[17]</sup> We assume in the following that  $\gamma_{\text{CML}/\text{COOH}} = 0$  mN m<sup>-1</sup>, as no hydrogen bonding or other chemical bonds should be formed. The resulting adhesion forces normalized to the radius  $F_{\text{JKR}}/R$  are compiled in the second column of Table 1. However, these

**Table 1.** Normalized adhesion forces compared to JKR- and Rabinovich-model.

	$F_{\text{exp}}/R$ [mN m <sup>-1</sup> ]	$F_{\text{JKR}}/R$ [mN m <sup>-1</sup> ]	$F_{\text{rough}}/R$ [mN m <sup>-1</sup> ]
CML/CH <sub>3</sub>	33.07 ± 10.54	169.65	12.81–41.78
CML/COOH	5.76 ± 3.91	56.55	4.27–13.93

values largely overestimate the adhesion forces in assuming a perfectly planar surface, while surface roughness has to be taken into account.<sup>[17,50,51]</sup> Here, the model of Rabinovich et al. has been applied.<sup>[52]</sup> The adhesion forces between rough surfaces are given by  $F_{\text{rough}} = \frac{3}{2}\pi W_{\text{adh}}R\rho/(R + \rho)$ . The roughness parameter  $\rho = \lambda^2/(58 r_{\text{RMS}})$  takes into account the mean peak-to-peak distance  $\lambda$  between surface asperities and the root mean square roughness of the surface  $r_{\text{RMS}}$ . Both values have been determined by imaging the surface topography of CML beads with a sharp AFM tip (see Supporting Information). We find  $\lambda = 20\text{--}40$  nm and  $r_{\text{RMS}} = 0.518 \pm 0.098$  nm. As the surface roughness of the template-assisted gold surface is significantly lower than for the CML particles, only the roughness of the particles has been considered. The last column with  $F_{\text{rough}}/R$  in Table 1 demonstrates that the experimentally determined forces not only match the ratio expected for the hydrophobic and hydrophilic regions, but also the absolute values of adhesion forces  $F_{\text{exp}}/R$  are in good agreement with the values predicted by the interfacial energies from the literature, when taking the surface roughness into account. The remaining discrepancies can be explained, if one takes into account that SAMs prepared by μCP have more defects than the ones obtained by immersion in solution due to reduced contact times.<sup>[53]</sup>

## 2.5. Soft Colloidal Probes in the Sub-μm Regime

The preparation of colloidal probes from soft particles represents a major challenge for the colloidal probe technique. In particular, core-shell (i.e., hard-soft) particles have been so far not accessible by the colloidal probe technique as the soft outer shell results in a highly flexible anchor for the particle and thus does not provide a rigid connection between probe and cantilever. So far, soft colloidal probes have been prepared only from rather large particles with diameters larger than 10 μm.<sup>[11,54,55]</sup> Here, we demonstrate for the first time the use of colloidal probes from core-shell particles in the sub-μm regime.

Thermo-responsive poly-*N*-isopropylacrylamide hydrogel (PNIPAM) shells with a solid silica core have been used as model system.<sup>[56–58]</sup> The core-shell particles have been prepared by seeded precipitation polymerization using surface-modified silica cores as seeds; further details are given in the Experimental Section.<sup>[57,59]</sup> A schematic drawing and a cryo-TEM (transmission electron microscopy) image of the particles are shown in Figure 6a.

PNIPAM-based hydrogels are stimuli responsive with respect to the external temperature and undergo a volume phase transition (VPT). This behavior is caused by the lower critical solution temperature of PNIPAM in water at temperatures of 32–33 °C.<sup>[60,61]</sup> Consequently, the thickness of the hydrogel shell of the core-shell particles in this study changes significantly when surpassing the VPT temperature (VPTT). This change has also been observed by mechanical measurements on the nm-scale,<sup>[62,63]</sup> where a morphological transition is taking place, leading to the collapse of the outer shell at elevated temperatures.<sup>[56]</sup> This morphological transition can be followed in situ by dynamic light scattering (DLS). Figure 6b shows the diameter of the core-shell particles as a function of the temperature. At 25 °C, the received particle diameter is in

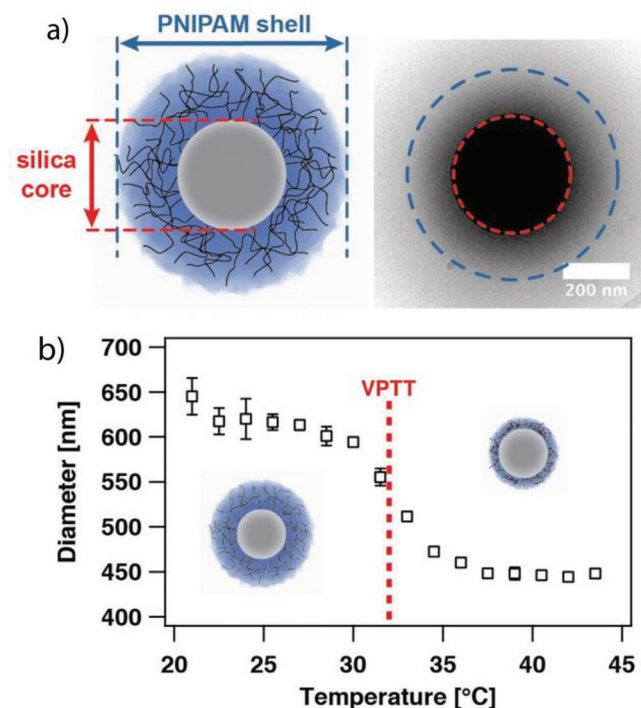


**Figure 6.** Properties of thermo-responsive core-shell particles. a) Schematic illustration and cryo-TEM image of a silica-PNIPAM core-shell particle. Dashed lines denote the approximate borders of core (red) and shell (blue), respectively. b) Temperature dependence of the particle diameter as determined by DLS.

good agreement with the results from the cryo-TEM image (see Figure 6a). In the vicinity of the VPTT (32 °C), a steep decrease in size is observed that levels off to a plateau at temperatures above 37 °C. The VPT has been reproducible throughout several temperature cycles for the core-shell particles (see the Supporting Information).

The silica-PNIPAM core-shell particles can be aspirated to a 300 nm sized aperture by the same procedure as for the CML particles (see Figure 1c). We assume that the soft outer hydrogel shell does not provide an obstacle to the aspiration. The PNIPAM shell shows a temperature-dependent behavior (see Figure 6) and Figure 7a illustrates in a schematic manner how the hydrogel shell of an aspirated colloidal particles would change as a function of the temperature. The conformational change of the PNIPAM shell has been followed by determining the change of mechanical properties as a function of the temperature. Single core-shell particles aspirated to the aperture have been used as colloidal probes and their interaction with the incompressible glass surface has been determined. Figure 7b shows some exemplary force versus distance curves at different temperatures, namely, 25 °C for a fully swollen PNIPAM shell and 41 °C for the fully collapsed state, respectively. Independent of the solution temperature, forces due to the electrosteric interaction and deformation of the outer shell are dominating the force profiles. For comparison, the bare silica cores (see Figure 7b, gray curve), which can be considered as incompressible, are interacting solely by long-range DLVO-type interactions similar to the CML particles. A constant aspiration

pressure of –200 mbar has been utilized for all temperatures. We could not observe desorption of the core-shell particles at any temperature and assume therefore that at this pressure the compression of the PNIPAM hydrogel is sufficiently strong to provide an immobilization of the particle at the aperture. In how far the soft hydrogel shell is providing an active “seal” that changes its shape and thus its permeability with temperature will be subject to further studies.

The repulsive forces between the silica core and the glass surface are resulting from the overlap of their respective diffuse layers.<sup>[15,25,64]</sup> However, these forces are much weaker than the electrosteric interactions between the outer PNIPAM shell and the glass surface. Silica particles as well as glass are negatively charged at pH 6 as reported in the literature.<sup>[26]</sup> Moreover, the force profiles for core-shell particles and the core, respectively, decay differently. The latter is given by screening effects, i.e., the Debye-length, of the electrolyte solution while the former includes also steric contributions. Only at very large separation distances, when no steric interactions are possible, the decay length for the core-shell particles corresponds approximately to the Debye-length.

## 2.6. Temperature Dependence for PNIPAM Core-Shell Particles on the Single Particle Level

At temperatures below the VPTT (here 25 °C), the PNIPAM hydrogel is in a highly swollen and thus soft state. Water represents a good solvent under this condition. Hence, the outer shell can be easily compressed and the core-shell particles behave as relatively soft materials in this temperature range.<sup>[56,60]</sup> The resulting mechanical response manifests itself by the low slope in the contact region of the force versus distance curves and an onset of compression at rather large distances (see blue curve at 25 °C in Figure 7b). By contrast, at elevated temperatures, the PNIPAM shell collapses and water, which is now acting as a bad solvent, is expelled from the shell (see red curve at 41 °C in Figure 7b). Hence, the shell material becomes stiffer and the slope in the contact region of the force versus distance curve gets steeper. At higher temperatures, the compression and steric response of the shell takes place at smaller probe-sample separations. The mechanical properties of PNIPAM hydrogels have been studied previously, albeit by indentation with a bare AFM-tip into single homogenous particles or films.<sup>[62,65–67]</sup>

Figure 7c summarizes a large number of force profiles acquired at different temperatures for a single silica-PNIPAM core-shell particle. The force profiles of the interaction of one specific PNIPAM core-shell particle against a glass surface at pH 6 are shown in a semi-logarithmic representation. Increasing the temperature around the range of the VPTT leads to a gradually decreasing interaction range due to the shrinking of the outer hydrogel shell. This finding is in line with the results for the particle diameter obtained by DLS (see Figure 6b).

While the slope of the force profiles remains nearly constant for interaction forces < 0.1 nN and thus large separation distances, the slope increases with temperature for >1 nN (i.e., the high force regime). The lower and intermediate force regime is dominated by electrosteric interactions. Only for very large separation distances when the PNIPAM shell has

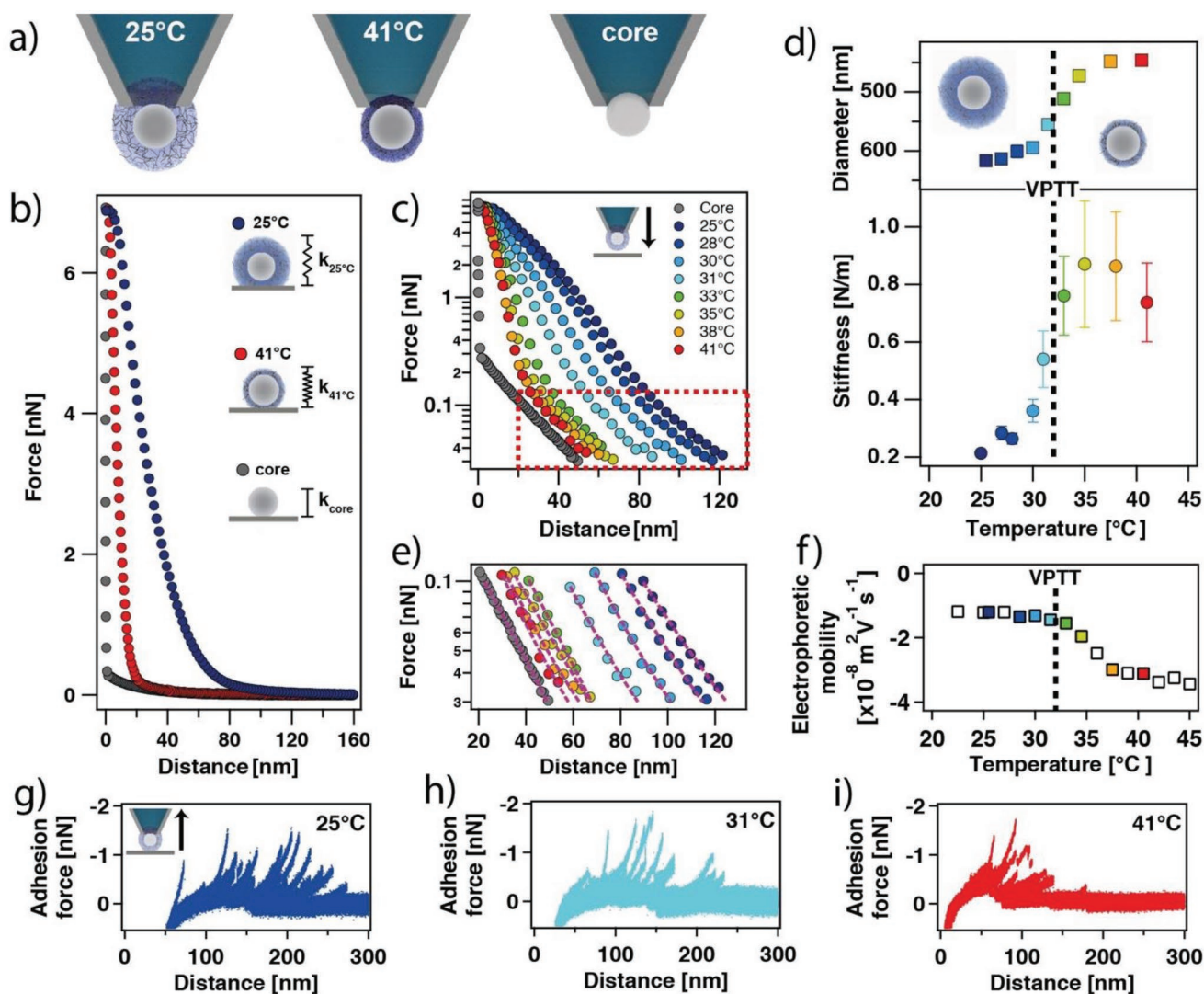


**Figure 7.** Mechanical properties of silica-PNIPAM core-shell particles. a) Schematic representation of core-shell particles aspirated at the aperture of a micro-channelled cantilever. b) Approach part of the force profiles for a core-shell particle at temperatures below and above the VPTT and for a bare silica core, respectively. Data have been acquired at pH 6 and  $I = 0.1 \times 10^{-3}$  M against a bare glass surface. c) Semi-logarithmic representation of force profiles acquired at different temperatures under similar conditions as in (b). d) Stiffness as obtained for the high force regime (i.e.,  $>1$  nN) versus temperature. For comparison, also the corresponding particle diameters (squares) as determined by DLS experiments are shown. Same color indicates identical temperatures. The dashed line denotes the VPTT of the PNIPAM shell. e) Interaction forces at large separation distances with corresponding exponential fits for entirely electrostatic interaction. f) Electrophoretic mobility of the PNIPAM core-shell particles as a function of temperature. g–i) Retraction part of the force profiles showing the adhesion of the PNIPAM shell on the glass surface at temperatures of 25, 31, and 41 °C, respectively. Each dataset comprises ten consecutively acquired force profiles.

no contact with the glass surface, a purely electrostatic interaction is taking place. This interpretation is corroborated by decay lengths of  $22 \pm 2$  nm in this distance regime (see fits in Figure 7e), which corresponds to the one determined for the bare silica core alone. Only in the case of a bare silica core, a pure interaction by DLVO-forces with the glass surface can be observed.<sup>[64]</sup> The presence of a charged PNIPAM layer has been verified independently by means of measurements of the electrophoretic mobility (see Figure 7f). The observed change in mobility has to be mostly attributed to the conformational change in the PNIPAM layer as in this way the ion permeability is changing. The resulting variation in mobility is in agreement with Ohshima theory<sup>[68]</sup> for soft particles and has been

confirmed also for other soft colloidal particles with an ion-permeable shell.<sup>[25]</sup> Moreover, also the adhesive properties indicate a change in the extension of the PNIPAM shell with temperature (see Figure 7g–i). With increasing temperature, the rupture events take place at smaller separation between probe and substrate.

By contrast for the high force regime (i.e.,  $>1$  nN), the core-shell particles are already in contact with the glass surface and the force profile is dominated by the bulk elasticity of the PNIPAM shell. Here, the mechanical properties of the core-shell particles can be estimated by their elastic response in the high force regime rather than by indentation measurements due to several restrictions, such as the small thickness of

the PNIPAM shell and the difficulty of determining the contact point due to the electrosteric forces. We determine the effective stiffness of the hydrogel  $k_{\text{shell}}$  according to:  $k_{\text{shell}} = k_C \left( \frac{C_{\text{bare}}}{C_{\text{shell}}} - 1 \right)$ .<sup>[69]</sup> Here  $C_{\text{shell}}$  and  $C_{\text{bare}}$  are given by the cantilever deflection per piezo displacement as determined for the core-shell particles and for the practically incompressible glass surface, respectively. The spring constant  $k_C$  of the cantilever has been determined independently by standard procedures before or after the measurements.<sup>[70]</sup> The resulting change of the stiffness  $k_{\text{shell}}$  with temperature is summarized in Figure 7d. The stiffness increases with temperature and shows a sigmoidal dependence similar to the one observed for the change in diameter. In order to illustrate the strong correlation with the particle diameter, the values for the diameter of the silica-PNIPAM core-shell particles, as determined by DLS, are shown additionally in Figure 7d. For elevated temperatures, the stiffness increases while the particle diameter drops. Both parameters change most substantially around the VPTT (i.e.,  $\approx 32$  °C). Furthermore, both stiffness and diameter data reveal a pronounced plateau for temperatures above 35 °C, where the outer shell is fully collapsed. These findings corroborate that indeed the temperature dependence of the PNIPAM hydrogel shell is responsible for the observed change in elastic response. Moreover, the measurements are in agreement with AFM-based indentation measurements on homogenous PNIPAM particles or films.<sup>[62,65–67]</sup> With increasing temperature, a deswelling of the PNIPAM shell takes place, thus leading to a more dense and therefore stiffer outer shell. At the same time, the silica core is not changing its elastic properties at these moderate temperatures (a corresponding control experiment is given in the Supporting Information). This type of structural changes on the single particle level could be observed here for the first time. These measurements will be especially useful in order to elucidate the complex interaction mechanisms between such silica-PNIPAM core-shell particles at the air/water interface.<sup>[31,71]</sup>

### 3. Conclusion

Aspiration of colloidal particles, instead of gluing them onto the cantilever, provides a revolutionary concept for the preparation of colloidal probes due to its inherent universality in respect to diameter and chemical composition of the probe particles. The combination of nanofluidics with AFM allows to overcome several current limitations of the colloidal probe technique. We demonstrated that particles with diameters well below 500 nm can be utilized as colloidal probes. Moreover, their immobilization is independent from their surface chemistry as well as their mechanical properties. Additionally, the aspiration technique allows for a reversible attachment. Thus, a statistically relevant number of particles can be used for a set of measurements. Hence, the primary advantages of the well-established multiple-colloidal probe technique are conserved but the versatility in terms of suitable probe particles has been extended dramatically, in particular allowing for previously problematic types of particles such as very small particles and particles with soft outer shell, respectively, or even a combination of both.

### 4. Experimental Section

**Materials:** All aqueous solutions were prepared from water of Milli-Q grade (i.e., resistivity  $>18$  M $\Omega$  cm<sup>-1</sup>). The pH was adjusted by means of 1 M HCl (Titrisol, Merck) and 1 M KOH (Titrisol, Merck) solutions. The ionic strength was adjusted by addition of KCl (Bio Ultra, Sigma-Aldrich). Prior to use, all solutions were degassed for at least 30 min under vacuum and filtrated with a polyethersulfone syringe filter with a pore size of 0.22  $\mu$ m (Carl Roth GmbH & Co KG). Solutions of 1-hexadecanethiol (99%, Aldrich) and 16-mercaptohexadecanoic acid (90%, Aldrich) were prepared with ethanol of analytical grade (Carl Roth GmbH & Co KG). CML microspheres with an average diameter of 0.33  $\mu$ m were purchased from Molecular Probes. For the preparation of “classical” colloidal probes, CML particles with an average diameter of 5  $\mu$ m were used (Thermo Fischer Scientific).

**Characterization of CML Particles:** SEM measurements (Leo 1530 VP Gemini, Carl Zeiss) were performed at an accelerating voltage of 3.0 kV. A droplet of highly diluted particle suspension was allowed to dry on a piece of silica, which was then sputtered with a 1.3 nm thick layer of platinum (sputter coater 208 HR, Cressington) prior to the SEM measurements. Particle size distributions were determined from SEM images and by DLS measurements. For the later, disposable solvent-resistant micro cuvettes (ZEN0040, Malvern Panalytical Ltd.) were used. Measurements were carried out at an angle of 173° with a Zetasizer Nano-ZS (Malvern Panalytical Ltd.) Measurements of the electrophoretic mobility were performed with the same instrument and folded capillary zeta cells (DTS1070, Malvern Panalytical Ltd.)

**Synthesis of Silica-PNIPAM Core-Shell Particles:** Core-shell particles with a silica core and a PNIPAM shell were synthesized according to a previously published protocol.<sup>[59]</sup> Further details are given in the Supporting Information.

**Characterization of Silica-PNIPAM Core-Shell Particles:** For cryo-TEM, 2  $\mu$ L of the particle suspension was placed on a lacey carbon film coated copper grid (Science Services), which was hydrophilized beforehand by an air plasma glow discharge unit (30 s with 50 W on a Solarus 950 from Gatan). Subsequently, most of the liquid was removed with blotting paper in a Leica EM GP grid plunge device, leaving a thin film stretched over the lace holes in the saturated water atmosphere of the environmental chamber. The specimens were instantly shock frozen by rapid immersion into liquid ethane cooled to approximately 95–97 K by liquid nitrogen in the temperature-controlled freezing unit of the Leica EM GP. This temperature was monitored and kept constant in the chamber during all the sample preparation steps. The specimen was inserted into a cryotransfer holder (CT3500, Gatan) and transferred to a Zeiss / LEO EM922 Omega EFTEM (Zeiss Microscopy GmbH). Examinations were carried out at temperatures around 95 K. The TEM was operated at an acceleration voltage of 200 kV. Zero-loss filtered images (5 keV) were taken under reduced dose conditions (100–1000 e nm<sup>-2</sup>). All images were acquired digitally by a bottom mounted CCD camera system (Ultrascan 1000, Gatan) and processed with a digital imaging processing system (Digital Micrograph GMS 1.9, Gatan).

Particle size distribution and electrophoretic mobility for the silica-PNIPAM core-shell particles were obtained under temperature control in the range from 21 to 44 °C in disposable solvent-resistant micro cuvettes on a Zetasizer Nano-ZS (see characterization of CML particles).

**Preparation of Samples by  $\mu$ CP and Their Characterization:** Chemically heterogeneous samples were prepared on uniformly flat gold substrates fabricated by a template-assisted process as previously described.<sup>[17,72]</sup> A laterally defined surface modification was obtained by  $\mu$ CP of alkanethiolates using an elastomeric stamp.<sup>[43]</sup> The stamp was prepared by casting a structured silicon master with repetitive doughnut-like features of 20  $\mu$ m outer and 10  $\mu$ m inner diameter, respectively, (GeSIM) using poly-dimethylsiloxane pre-polymer (Sylgard 184, Sigma-Aldrich). After degassing the freshly prepared pre-polymer solution and distributing it over the silicon master, it was cured in an oven at 80 °C for 4 h. As “ink,” a  $5 \times 10^{-3}$  M solution of 1-hexadecanethiol in ethanol

was used. The wetted stamp was pressed onto the gold surface for about 20 s. The uncovered regions on the sample were modified with a  $5 \times 10^{-3}$  M solution of 16-mercaptohexadecanoic acid in ethanol by dip-coating for about 10 s. After  $\mu$ CP, the sample was thoroughly rinsed with ethanol and Milli-Q water and dried under nitrogen.

The thereby prepared chemically structured surfaces were characterized by three different techniques: i) condensation microscopy: images of the  $\mu$ CP sample were acquired mounted on a fixed-stage microscope (Examiner. D1, Carl Zeiss) using a purposely constructed peltier cooling stage. By cooling the sample below the dew point at around 5 °C, water condensation occurred first on the hydrophilic parts of the sample. ii) AFM-imaging in liquid by PeakForce mode: AFM images were acquired by PeakForce mode in liquid with a dimension ICON (Bruker) in electrolyte solution. Higher adhesion forces were observed on the hydrophobic regions of the sample as known from chemical force microscopy.<sup>[46]</sup> iii) SEM imaging: samples obtained by  $\mu$ CP showed a contrast in the SEM. Imaging was performed on a Hitachi Table Top SEM at 5 keV.

**Preparation of Colloidal Probes by Gluing:** For the preparation of “classical” colloidal probes, 5  $\mu$ m sized CML particles (Molecular Probes) were attached onto a tipless cantilever (CSC-37, Mikromasch) by means of UV-curable glue (NOA 63, Norland Products). A precise positioning of the particles was achieved using an optical microscope (Axio Examiner.D1, Carl Zeiss) equipped with a micromanipulator (DC-3 KS, Märzhäuser).

**Characterization of Cantilevers with an Internal Micro-Channel:** Micro-channeled cantilevers (FluidFM Nanopipette, Cytosurge AG) with a nominal aperture of 300 nm located at the apex of a pyramidal tip and a nominal spring constant of 0.6 N m<sup>-1</sup> were used throughout this study. The spring constant of each individual cantilever was calibrated by the added mass method,<sup>[70]</sup> where at least six different tungsten particles of various diameters were temporarily attached to the cantilever. The resulting shift in the resonant frequency of the cantilever was determined.<sup>[70]</sup> The mass of the particles was estimated by means of the diameter from optical microscopy (Axio Observer.Z1, Carl Zeiss) and the density of tungsten of 19.25 g cm<sup>-3</sup>.

SEM images of the micro-channeled cantilevers were acquired on a Leo 1530 VP Gemini (Carl Zeiss) with an accelerating voltage of 3.0 kV. Beforehand, the cantilevers were sputter-coated with a 1.3 nm layer of platinum (Sputter coater 208 HR, Cressington). Cross-sections through the micro-channel of the cantilever were obtained by FIB milling with a FIB Scios DualBeam SEM (Thermo Fisher Scientific) at an acceleration voltage of 30 kV and a beam current of about 0.3–0.5 nA.

**Direct Force Measurements:** The AFM experiments were conducted on a commercial AFM system from Nanosurf (Flex-FPM V5 head equipped with a SLD, Nanosurf AG). The AFM was mounted on an inverted optical microscope (Axio Observer.Z1, Carl Zeiss). The micro-channeled cantilevers were connected to a microfluidic pressure control unit (Cytosurge AG) allowing the reversible aspiration of single objects to the aperture. Prior to each experiment, the cantilever was treated with air plasma for 5 min (Zepto, Diener Electronics). After injecting about 40  $\mu$ L of degassed electrolyte solution in the reservoir of the micro-channeled cantilever, an overpressure of +1000 mbar was applied for 2 min to fill the microfluidic channel. Complete filling was verified by the shift of the cantilevers resonance frequency and by optical microscopy, respectively. Particles were aspirated to the aperture, while the cantilever was immersed in the diluted particle suspension in direct vicinity (<100  $\mu$ m) of the sample surface. A successful particle aspiration was detected by a method previously proposed by Helfrich et al., which was based on the continuous acquisition of force versus distance curves toward a sample surface, while applying an aspiration pressure of about –600 mbar.<sup>[15,17]</sup>

Chemically structured ( $\mu$ CP) samples were attached to the glass ground of a glass bottom dish (Willco Wells BV) by means of UV-curable epoxy glue (NOA63, Norland Optical Adhesives). Experiments with PNIPAM core-shell particles were carried out in a commercial AFM fluid cell with active temperature control (BioHeater, Asylum Research). Substrate was here a rigid glass surface consecutively cleaned by ethanol,

Milli-Q water, snow-jet (Tectra), and 10 min of air plasma (Zepto, Diener Electronics, Ebhausen, Germany).

In order to determine the optical lever sensitivity of the cantilevers during the experiments, a thin glass slide was attached onto the glass sample by means of UV-curable epoxy glue (NOA63, Norland Optical Adhesives). In general, force curves were acquired with a ramping speed of 500 nm s<sup>-1</sup> and a maximum loading deflection of 0.15 V. Raw data (deflection vs displacement) were converted to force versus distance curves by standard algorithms<sup>[2,3]</sup> implemented in custom-written procedures in IgorPro (Wavemetrics Inc.).<sup>[15]</sup> If not stated otherwise, all force versus distance curves were averaged from at least 40 individual curves acquired at the same position of the sample. Mapping of the adhesion forces was performed by acquiring force curves on a 20  $\times$  20 positional grid (dimension 50  $\mu$ m  $\times$  50  $\mu$ m). The resulting adhesion maps were calculated from the absolute adhesion minimum of each individual curve. The corresponding procedures were written in IgorPro.

## Supporting Information

Supporting Information is available from the Wiley Online Library or from the author.

## Acknowledgements

The authors thank Patrick Knödler and Markus Lippitz (both University of Bayreuth, Chair of Experimental Physics III) for the FIB-milling of the micro-channeled cantilever. Carmen Kunert helped with the SEM measurements and Markus Drechsler with the cryo-TEM measurements. The authors thank the German Research Foundation (DFG) for financial support in the framework of the SFB 840.

## Conflict of Interest

The authors declare no conflict of interest.

## Keywords

atomic force microscopy, colloidal probes, colloids, nanofluidics, surface forces

Received: June 7, 2019  
Revised: August 18, 2019  
Published online: September 23, 2019

- [1] J. Israelachvili, *Intermolecular and Surface Forces*, Academic Press, San Diego, CA 1991.
- [2] T. J. Senden, *Curr. Opin. Colloid Interface Sci.* **2001**, *6*, 95.
- [3] H.-J. Butt, B. Cappella, M. Kappl, *Surf. Sci. Rep.* **2005**, *59*, 1.
- [4] H. J. Butt, R. Berger, E. Bonaccorso, Y. Chen, J. Wang, *Adv. Colloid Interface Sci.* **2007**, *133*, 91.
- [5] M. Borkovec, I. Szilagyi, I. Popa, M. Finessi, P. Sinha, P. Maroni, G. Papastavrou, *Adv. Colloid Interface Sci.* **2012**, *179–182*, 85.
- [6] J. Israelachvili, Y. Min, M. Akbulut, A. Alig, G. Carver, W. Greene, K. Kristiansen, E. Meyer, N. Pesika, K. Rosenberg, H. Zeng, *Rep. Prog. Phys.* **2010**, *73*, 036601.
- [7] H.-J. Butt, *Biophys. J.* **1991**, *60*, 1438.
- [8] W. A. Ducker, T. J. Senden, R. M. Pashley, *Nature* **1991**, *353*, 239.
- [9] R. Pericet-Camara, G. Papastavrou, S. H. Behrens, M. Borkovec, *J. Phys. Chem. B* **2004**, *108*, 19467.

- [10] I. Popa, P. Sinha, M. Finessi, P. Maroni, G. Papastavrou, M. Borkovec, *Phys. Rev. Lett.* **2010**, *104*, 228301.
- [11] D. Pussak, D. Ponader, S. Mosca, T. Pompe, L. Hartmann, S. Schmidt, *Langmuir* **2014**, *30*, 6142.
- [12] N. Helfricht, E. Doblhofer, V. Bieber, P. Lommes, V. Sieber, T. Scheibel, G. Papastavrou, *Soft Matter* **2017**, *13*, 578.
- [13] S. Rentsch, R. Pericet-Camara, G. Papastavrou, M. Borkovec, *Phys. Chem. Chem. Phys.* **2006**, *8*, 2531.
- [14] I. Popa, G. Papastavrou, M. Borkovec, *Macromolecules* **2010**, *43*, 1129.
- [15] N. Helfricht, A. Mark, L. Dorwling-Carter, T. Zambelli, G. Papastavrou, *Nanoscale* **2017**, *9*, 9491.
- [16] M. Kappl, H.-J. Butt, *Part. Part. Syst. Charact.* **2002**, *19*, 129.
- [17] V. Kuznetsov, G. Papastavrou, *Langmuir* **2012**, *28*, 16567.
- [18] M. Chyashnavichyus, S. L. Young, R. Geryak, V. V. Tsukruk, *Polymer* **2016**, *102*, 317.
- [19] M. E. McConney, S. Singamaneni, V. V. Tsukruk, *Polym. Rev.* **2010**, *50*, 235.
- [20] Y. Gan, *Rev. Sci. Instrum.* **2007**, *78*, 081101.
- [21] C. C. Yuan, D. Zhang, Y. Gan, *Rev. Sci. Instrum.* **2017**, *88*, 031101.
- [22] V. Kuznetsov, G. Papastavrou, *Rev. Sci. Instrum.* **2012**, *83*, 116103.
- [23] A. Meister, M. Gabi, P. Behr, P. Studer, J. Vörös, P. Niedermann, J. Bitterli, J. Polesel-Maris, M. Liley, H. Heinzelmann, T. Zambelli, *Nano Lett.* **2009**, *9*, 2501.
- [24] P. Dörig, D. Ossola, A. M. Truong, M. Graf, F. Stauffer, J. Vörös, T. Zambelli, *Biophys. J.* **2013**, *105*, 463.
- [25] N. Helfricht, E. Doblhofer, J. F. L. Duval, T. Scheibel, G. Papastavrou, *J. Phys. Chem. C* **2016**, *120*, 18015.
- [26] M. Kobayashi, M. Skarba, P. Galletto, D. Cakara, M. Borkovec, *J. Colloid Interface Sci.* **2005**, *292*, 139.
- [27] M. M. H. Ayoub, *Pigm. Resin Technol.* **1997**, *26*, 6.
- [28] M. S. El-Actsser, J. Tang, X. Wang, E. S. Daniels, V. L. Dimonie, E. D. Sudol, *J. Coat. Technol.* **2001**, *73*, 51.
- [29] C. D. Anderson, E. S. Daniels, *Emulsion Polymerisation and Latex Applications*, Rapra Review Reports 14, Rapra Technology Limited, Shawbury, Shrewsbury, Shropshire **2003**.
- [30] A. S. El-Tawary, D. Stock, M. Gallei, W. A. Ramadan, M. A. Shams El-Din, G. Reiter, R. Reiter, *Langmuir* **2018**, *34*, 3909.
- [31] S. A. Vasudevan, A. Rauh, M. Kröger, M. Karg, L. Isa, *Langmuir* **2018**, *34*, 15370.
- [32] S. A. Vasudevan, A. Rauh, L. Barbera, M. Karg, L. Isa, *Langmuir* **2018**, *34*, 886.
- [33] M. Karg, T. Hellweg, P. Mulvaney, *Adv. Funct. Mater.* **2011**, *21*, 4668.
- [34] L. Nyström, M. Malmsten, *Adv. Colloid Interface Sci.* **2016**, *238*, 88.
- [35] C.-F. Lee, T.-H. Young, Y.-H. Huang, W.-Y. Chiu, *Polymer* **2000**, *41*, 8565.
- [36] J. Tang, E. S. Daniels, V. L. Dimonie, M. S. Vratsanos, A. Klein, M. S. El-Aasser, *J. Appl. Polym. Sci.* **2002**, *86*, 2788.
- [37] C. D. Bain, G. M. Whitesides, *Langmuir* **1989**, *5*, 1370.
- [38] V. Kane, P. Mulvaney, *Langmuir* **1998**, *14*, 3303.
- [39] R. Schweiss, C. Werner, W. Knoll, *J. Electroanal. Chem.* **2003**, *540*, 145.
- [40] D. R. Lide, *CRC Handbook of Chemistry and Physics*, 85th ed., CRC Press, Boca Raton, FL **2004**.
- [41] M. A. Bryant, R. M. Crooks, *Langmuir* **1993**, *9*, 385.
- [42] S. H. Behrens, D. I. Christl, R. Emmerzael, P. Schurtenberger, M. Borkovec, *Langmuir* **2000**, *16*, 2566.
- [43] Y. Xia, G. M. Whitesides, *Annu. Rev. Mater. Sci.* **1998**, *28*, 153.
- [44] G. Papastavrou, S. Akari, *Nanotechnology* **1999**, *10*, 453.
- [45] W. F. Heinz, J. H. Hoh, *Biophys. J.* **1999**, *76*, 528.
- [46] P. Warszyński, G. Papastavrou, K. D. Wantke, H. Möhwald, *Colloids Surf. A* **2003**, *214*, 61.
- [47] S. K. Sinniah, A. B. Steel, C. J. Miller, J. E. Reutt-Robey, *J. Am. Chem. Soc.* **1996**, *118*, 8925.
- [48] A. Noy, D. V. Zezenov, C. M. Lieber, *Annu. Rev. Mater. Sci.* **1997**, *27*, 381.
- [49] D. V. Zezenov, A. Noy, P. Ashby, *J. Adhes. Sci. Technol.* **2005**, *19*, 313.
- [50] C. S. Hodges, J. A. S. Cleaver, M. Ghadiri, R. Jones, H. M. Pollock, *Langmuir* **2002**, *18*, 5741.
- [51] E. R. Beach, G. W. Tormoen, J. Drelich, R. Han, *J. Colloid Interface Sci.* **2002**, *247*, 84.
- [52] Y. I. Rabinovich, J. J. Adler, A. Ata, R. K. Singh, B. M. Moudgil, *J. Colloid Interface Sci.* **2000**, *232*, 17.
- [53] J. A. Helmuth, H. Schmid, R. Stutz, A. Stemmer, H. Wolf, *J. Am. Chem. Soc.* **2006**, *128*, 9296.
- [54] R. Buzio, U. Valbusa, *J. Phys.: Condens. Matter* **2008**, *20*, 354014.
- [55] R. Buzio, A. Bosca, S. Krol, D. Marchetto, S. Valeri, U. Valbusa, *Langmuir* **2007**, *23*, 9293.
- [56] M. Karg, I. Pastoriza-Santos, L. M. Liz-Marzán, T. Hellweg, *ChemPhysChem* **2006**, *7*, 2298.
- [57] M. Karg, S. Wellert, S. Prevost, R. Schweins, C. Dewhurst, L. M. Liz-Marzán, T. Hellweg, *Colloid Polym. Sci.* **2011**, *289*, 699.
- [58] A. Rauh, M. Rey, L. Barbera, M. Zanini, M. Karg, L. Isa, *Soft Matter* **2017**, *13*, 158.
- [59] A. Rauh, T. Honold, M. Karg, *Colloid Polym. Sci.* **2016**, *294*, 37.
- [60] M. Karg, T. Hellweg, *Curr. Opin. Colloid Interface Sci.* **2009**, *14*, 438.
- [61] S. Wellert, M. Richter, T. Hellweg, R. von Klitzing, Y. Hertle, *Z. Phys. Chem.* **2015**, *229*, 1225.
- [62] S. Schmidt, M. Zeiser, T. Hellweg, C. Duschl, A. Fery, H. Möhwald, *Adv. Funct. Mater.* **2010**, *20*, 3235.
- [63] J. Dubbert, K. Nothdurft, M. Karg, W. Richtering, *Macromol. Rapid Commun.* **2015**, *36*, 159.
- [64] S. H. Behrens, D. G. Grier, *J. Chem. Phys.* **2001**, *115*, 6716.
- [65] X. Sui, Q. Chen, M. A. Hempenius, G. J. Vancso, *Small* **2011**, *7*, 1440.
- [66] O. Tagit, N. Tomczak, G. J. Vancso, *Small* **2008**, *4*, 119.
- [67] A. Burmistrova, M. Richter, C. Uzum, R. V. Klitzing, *Colloid Polym. Sci.* **2011**, *289*, 613.
- [68] H. Ohshima, *Colloids Surf., A* **2014**, *440*, 151.
- [69] W. A. Ducker, Z. Xu, J. N. Israelachvili, *Langmuir* **1994**, *10*, 3279.
- [70] J. P. Cleveland, S. Manne, D. Bocek, P. K. Hansma, *Rev. Sci. Instrum.* **1993**, *64*, 403.
- [71] J. S. J. Tang, R. S. Bader, E. S. A. Goerlitzer, J. F. Wendisch, G. R. Bourret, M. Rey, N. Vogel, *ACS Omega* **2018**, *3*, 12089.
- [72] D. Stamou, D. Gourdon, M. Liley, N. A. Burnham, A. Kulik, H. Vogel, C. Duschl, *Langmuir* **1997**, *13*, 2425.